AGU PUBLICATIONS

Geochemistry, Geophysics, Geosystems

RESEARCH ARTICLE
10.1002/2015GC005882

Key Points:
- Three anisotropic layers in NZ South Island and near offshore
- Broad zone of plate-boundary shear in lithosphere near southern Alpine Fault
- This widely distributed deformation agrees with the thin viscous sheet model

Correspondence to:
S. C. Karalliyadda,
sapi.karal@outlook.com

Citation:
Karalliyadda, S. C., M. K. Savage, A. Sheehan, J. Collins, D. Zietlow, and A. Shelley (2015), S-wave splitting in the offshore South Island, New Zealand: Insights into plate-boundary deformation, *Geochem. Geophys. Geosyst.*, *16*, 2829–2847, doi:10.1002/2015GC005882.

Received 27 APR 2015
Accepted 2 AUG 2015
Accepted article online 6 AUG 2015
Published online 30 AUG 2015

© 2015. American Geophysical Union. All Rights Reserved.

S-wave splitting in the offshore South Island, New Zealand: Insights into plate-boundary deformation

S. C. Karalliyadda[1], M. K. Savage[1], A. Sheehan[2], J. Collins[3], D. Zietlow[2], and A. Shelley[1]

[1]Institute of Geophysics, Victoria University of Wellington, Wellington, New Zealand, [2]Department of Geological Sciences, University of Colorado at Boulder, Boulder, Colorado, USA, [3]Woods Hole Oceanographic Institution, Woods Hole, Massachusetts, USA

Abstract Local and regional S-wave splitting in the offshore South Island of the New Zealand plate-boundary zone provides constraints on the spatial and depth extent of the anisotropic structure with an enhanced resolution relative to land-based and SKS studies. The combined analysis of offshore and land measurements using splitting tomography suggests plate-boundary shear dominates in the central and northern South Island. The width of this shear zone in the central South Island is about 200 km, but is complicated by stress-controlled anisotropy at shallow levels. In northern South Island, a broader (>200 km) zone of plate-boundary parallel anisotropy is associated with the transitional faulting between the Alpine fault and Hikurangi subduction and the Hikurangi subduction zone itself. These results suggest S-phases of deep events (~90 km) in the central South Island are sensitive to plate-boundary derived NE-SW aligned anisotropic media in the upper-lithosphere, supporting a "thin viscous sheet" deformation model.

1. Introduction

The study of internal deformation at plate-boundaries enables us to understand how lithospheric blocks interact with each other. An oblique-convergent boundary between the Australian-Pacific (AUS-PAC) plates evolved since the Eocene (~40 Ma) [*Cox and Sutherland*, 2007]. In South Island, this plate-boundary was initiated as a passive margin and it was later transformed to a large strike-slip fault (Alpine fault) [*Sutherland*, 1999]. A fault offset of 450 km has accumulated as a result of both pure and oblique strike-slip movements of the AUS-PAC plates over the last 25 My. Present-day plate-boundary configuration in the South Island is characterized by the transpressional Alpine fault that interlinks the Hikurangi and Puysegur subduction zones (Figure 1a). This plate-boundary fault zone is an ideal location to explore lithospheric deformation associated with continental margins because of its present-day transpressional behavior and historic pure strike-slip nature.

1.1. Constraining Plate-Boundary Deformation Via Shear-Wave Splitting

Lattice preferred orientation of minerals creates an anisotropic medium with directional variations of its physical properties. This has been considered as the main source of anisotropy in the upper mantle, asthenosphere and perhaps in the lower-crust [*Savage*, 1999]. Anisotropy in the upper-mid crust is largely due to stress controlled sources such as aligned micro-cracks, or fluid-filled cracks, and structural sources like macro-faults and the alignment of bedding planes and foliations [*Boness and Zoback*, 2004]. Anisotropy is an excellent indicator of strain (or deformation) distribution at plate-boundaries [*Skemer et al.*, 2012] and it helps to delineate deformation kinematics and understand the rheology of the system [*Karato et al.*, 1989].

Vauchez and Nicolas [1991] hypothesized that large-scale displacement in plate-boundary faults is likely associated with deformation in the whole lithosphere, and is characterized by broadly distributed shear deformation on either sides of the fault. The depth distribution of this deformation, however, depends on the mechanical coupling between layers [*Flesch et al.*, 2005]. Shearing of intrinsically anisotropic minerals (e.g., olivine, pyroxene) in the lithosphere and asthenosphere in response to the fault displacement results in lattice preferred orientation with horizontal mineral alignment on vertical flow planes (or steep foliations) that are parallel to the plate-boundary [*Nicolas and Christensen*, 1987]. The width of this anisotropic zone is, therefore, a measure of distributed shear deformation associated with the transcurrent fault movement. As

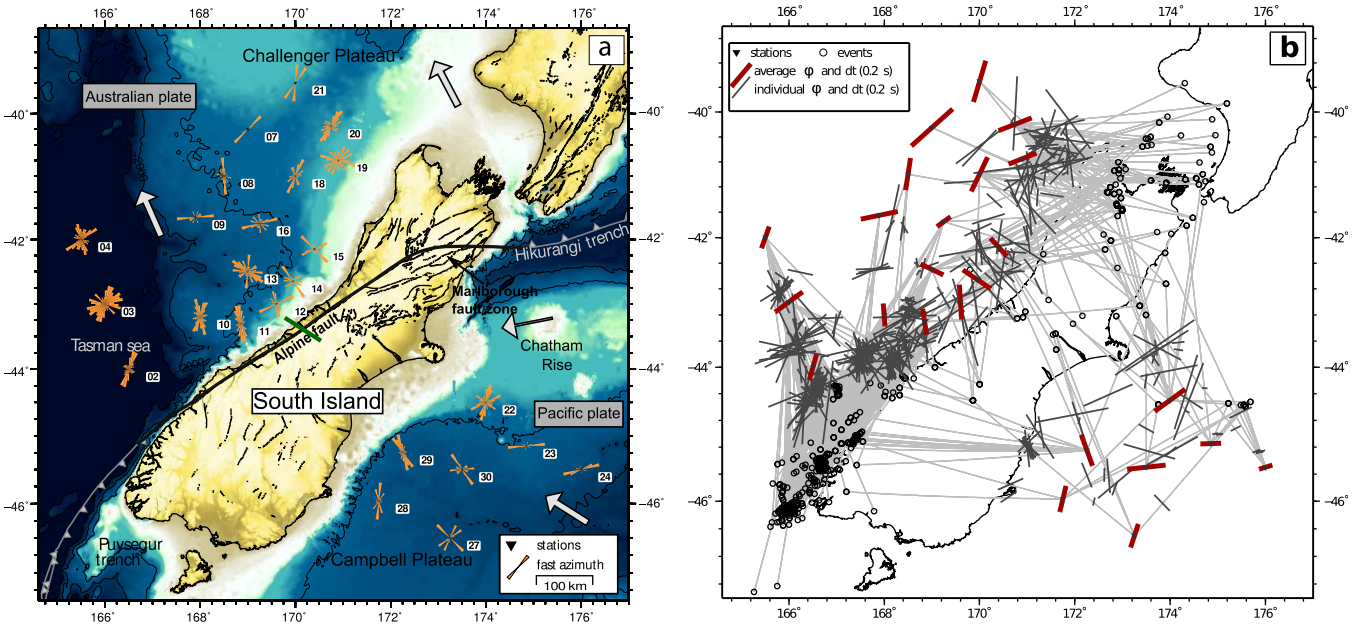

Figure 1. (a) Offshore study region of the South Island and circular histograms of fast azimuth plotted at the OBS station (numbers denote the station names) locations. Bold and thin arrows indicate the absolute and relative plate motion directions, respectively. The green bar on the Alpine fault denotes the approximate SH_{max} direction in the central South Island (~115°) [*Boese et al.*, 2012]. (b) Ray path distribution (light gray lines) and event locations of the measurements that satisfy the best filter and highest grade quality criteria (Appendix A). Individual splitting measurements (gray bars) are plotted at one-quarter of the epicentral distance that is measured from the station. Red bars indicate the average station δt and ϕ. Both red and gray bars are scaled by δt.

suggested by *Otsuki* [1978], 500–1000 km of fault displacement can produce deformation of a few kilometers to ~40 km width in the lithospheric mantle and mid lower-crust. If this deformation is partitioned into several major shear zones in the midlower crust, such zones will have a single large-scale shear zone in the mantle lithosphere and, therefore, distributed deformation ($\geq$ 100 km) occurs around the plate-boundary [*Nicolas*, 1993].

Previous studies of P_n anisotropy [*Scherwath et al.*, 2002; *Baldock and Stern*, 2005], P-wave delays [*Molnar et al.*, 1999; *Stern et al.*, 2000] and SKS splitting [*Klosko et al.*, 1999] in South Island suggest that the mantle shear zone that is associated with the Alpine fault is distributed in a ~200–300 km broad area around the plate-boundary and may extend into offshore regions of the South Island. Offshore SKS splitting measurements by *Zietlow et al.* [2014] found plate-boundary subparallel shear within 100 km west of the central Alpine fault. Land stations also revealed plate-boundary subparallel shear within ~100 km east of the fault, but offshore of the east coast no plate-boundary controlled shear was observed (section 2.3). Geodetic estimations and finite-element modeling suggest that deformation is confined to a zone about 80–100 km from the fault [*Beavan et al.*, 1999; *Ellis et al.*, 2006; *Moore et al.*, 2002]. Finite strain estimations from geological markers [*Little et al.*, 2002] also found higher strain accumulation toward the plate-boundary (east to west), indicating crust-mantle coupling toward the fault. Lack of depth resolution of SKS splitting does not allow one to distinguish between anisotropy in the lithosphere and asthenosphere using SKS phases. For this reason, *Karalliyadda and Savage* [2013] carried out a local shear-wave (S-wave) splitting investigation using stations on South Island to examine lithospheric anisotropy. Despite the complex nature of splitting from high-frequency local S-waves, the study found that the mantle shear zone due to plate-boundary deformation is distributed within ~130 km of the boundary in the central South Island and may be more distributed in the northern South Island than in the central South Island. The study also noticed that high-frequency local S-phases are more sensitive to crustal stress-induced anisotropy in some regions of South Island.

Here we extend the study by *Karalliyadda and Savage* [2013] into offshore South Island to investigate seismic anisotropy in the previously unexplored offshore regions of South Island using local/regional S-wave splitting. S-wave birefringence (i.e., splitting of S-wave into two quasi S-phases) is a characteristic property of S-waves propagating in an anisotropic medium. Splitting occurs in such a way that the polarization

direction of the faster S-wave (fast azimuth or direction-ϕ) is parallel to the alignment of the anisotropic medium and the slower S-wave is orthogonal to the polarization direction of the fast S-wave. The time separation (delay time-δt) acquired by the two quasi S-phases upon propagating in the anisotropic medium gives information on the strength and spatial extent of anisotropy. We estimate these S-wave splitting parameters (i.e., ϕ and δt) from regional and local events recorded on the ocean-bottom seismographs to constrain the spatial distribution of splitting parameters. We also aim to address the question of whether the local/regional splitting in this region is entirely governed by the plate-boundary deformation or by other means.

2. Splitting Parameters From OBS Data

2.1. Data and Method

Twenty eight broadband Ocean Bottom Seismographs (OBS) that were deployed in the eastern and western offshore regions of the South Island as a part of the MOANA (Marine Observation of Anisotropy Near Aotearoa) experiment [(J. A. Collins et al., unpublished MOANA Recovery Cruise Report, 2010); *Yang et al*., 2012] were used to retrieve S-phases from local and regional events. OBS on the western side were distributed in both the shallow (Challenger Plateau) and deep ocean (Tasman sea). Eastern side OBS were located on the Campbell Plateau and Chatham Rise (Figure 1a). Seismicity in the area was mostly distributed outside of the OBS network, roughly centered between the western and eastern OBS deployments (open circles in Figure 1b show the events that yielded a good quality splitting measurements). The majority of events were distributed along the plate boundary between 2 and 240 km depth. Deep events mostly occurred within the two subducting slabs and shallow events were in the crust. Most of the OBS stations have a limited backazimuthal coverage, therefore, the deeper structure is only sampled by the events from certain back azimuths. We used the GeoNet catalog for the period from February 2009 to January 2010 to determine events and used the origin times to extract the events from OBS records. Waveforms recorded on OBS stations were corrected for the OBS orientations using the rotation angles estimations of *Stachnik et al*. [2012]. Approximately 2000 S-phases were used to determine S-wave splitting on OBS stations in the eastern and western sides from S-phases with magnitude ≥ 3.0 and ≥ 3.5, respectively. Hand picked S-phases were analyzed for splitting with the automated S-wave splitting technique of MFAST [*Wessel*, 2010; *Savage et al*., 2010]. MFAST uses the eigenvalue minimization and cluster analysis methods introduced by *Silver and Chan* [1991] and *Teanby et al*. [2004b] (Figure B1 in Appendix B), respectively. S-waves were filtered using two-pole Butterworth bandpass filters with 14 different corner frequencies, ranging between 0.4 Hz and 10 Hz frequencies [*Savage et al*., 2010]. Then the product of the signal-to-noise ratio (SNR) and bandwidth of the filtered S-wave analysis window were determined. For each S-wave, Mfast selected three filtered S-wave analysis windows with the highest SNR-bandwidth product to determine splitting measurements. Details are in Appendix A and in *Savage et al*. [2010]. We eliminated poor quality events and/or measurements in three steps: (i) events with ambiguous and/or distorted S-wave impulses were avoided prior to splitting analysis, (ii) signals with low SNR ($\leq$ 2) were avoided during the analysis and, (iii) poor quality measurements were eliminated by either visual inspection of splitting parameters on diagnostic plots (e.g., particle motion plots, contour diagrams and wave-form plots) or by applying the highest quality grading criteria that comes with the MFAST program (appendix A). We noticed that waveforms and/or splitting measurements of the farthest stations (NZ05, NZ06, and NZ 26) do not satisfy the above quality criteria and, thus, those stations did not yield any acceptable splitting measurements. About 1540 measurements were graded as AB quality (i.e., good quality splitting measurements, based on the clustering analysis comparison of measurements from different measurement windows. See appendix A for quantitative information about the grading criteria). The spatial variations of splitting parameters were evaluated from 1300 measurements that satisfied the high quality grading criteria (Table B1), which meant they were nonnull measurements with dense error contours and small splitting errors (see appendix A for specific explanations).

Volti et al. [2005] emphasized that the S-wave window (SWW) used for splitting in the sea-floor can be deviated from the limits of usual SWW (incidence angle $\leq 35^{\circ}$) that applies in the onshore splitting analysis. As a result of the low-velocity unconsolidated sediment layers in the sea floor [*Tsuji et al*., 2011], high-frequency local and regional S-waves attain almost vertical incidence as they reach the sea-floor [*Volti et al*., 2005] and, therefore, splitting measurements are unaffected by the distorted S-arrivals owing to phase conversions [*Booth and Crampin*, 1985; *Nuttli*, 1961] at the sea-floor. With careful inspection of splitting

Table 1. Measurements and Statistics of Offshore Splitting Measurements Shown in Figure 2

Station	ST-AF (km)[a]	no	$\bar{\phi}$[b]	$SE_{\bar{\phi}}$[c]	$CSD_{\bar{\phi}}$[d]	$error_{\bar{\phi}}$[e]	R	Mean δt	$SE_{\delta t}$[f]	$SD_{\delta t}$	$error_{\delta t}$[e]
NZ02	116.79	81	16	8	46	2.6	0.283	0.18	0.02	0.16	0.004
NZ03	224.52	42	54	16	52	3.9	0.195	0.23	0.03	0.18	0.007
NZ04	338.50	21	19	14	44	1.9	0.313	0.15	0.02	0.08	0.003
NZ07	387.18	2	48	4	5	0.1	0.985	0.38	0.02	0.03	0.005
NZ08	296.54	6	8	17	36	1.4	0.464	0.22	0.09	0.21	0.004
NZ09	263.04	4	78	4	8	0.7	0.961	0.26	0.02	0.03	0.007
NZ10	111.47	97	−4	7	45	2.9	0.290	0.15	0.01	0.11	0.004
NZ11	65.34	79	−9	6	39	2.0	0.389	0.17	0.01	0.11	0.004
NZ12	61.13	15	−4	21	48	2.8	0.248	0.23	0.04	0.18	0.013
NZ13	134.98	47	−64	10	45	2.7	0.285	0.17	0.02	0.14	0.003
NZ14	77.28	14	−56	19	46	1.3	0.273	0.23	0.04	0.17	0.005
NZ15	101.86	8	−42	18	40	2.5	0.376	0.16	0.03	0.10	0.006
NZ16	192.30	11	54	35	54	3.1	0.174	0.10	0.03	0.09	0.003
NZ18	226.76	15	25	23	49	2.6	0.226	0.26	0.05	0.18	0.005
NZ19	193.44	25	68	41	62	2.5	0.098	0.20	0.03	0.16	0.005
NZ20	248.38	21	69	14	44	2.2	0.306	0.24	0.03	0.13	0.004
NZ21	349.08	2	16	10	14	0.2	0.891	0.29	0.24	0.34	0.006
NZ22	276.66	15	54	23	50	4.3	0.222	0.26	0.06	0.22	0.011
NZ23	374.95	6	88	12	28	4.7	0.611	0.13	0.07	0.21	0.003
NZ24	463.27	6	73	6	14	1.0	0.884	0.08	0.02	0.05	0.003
NZ27	421.65	4	18	20	35	3.4	0.465	0.16	0.06	0.11	0.005
NZ28	305.93	5	13	23	40	0.7	0.372	0.18	0.03	0.06	0.007
NZ29	263.41	17	−20	10	36	1.9	0.455	0.22	0.03	0.12	0.006
NZ30	343.98	4	84	17	32	1.6	0.533	0.26	0.08	0.17	0.009

[a]Distance from the Alpine Fault to station.
[b]Mean ϕ.
[c]Standard error of $\bar{\phi}$.
[d]Circular standard deviation of the $\bar{\phi}$.
[e]Average errors of the individual ϕ and δt errors [*Silver and Chan*, 1991] at each station.
[f]Standard error of the mean δt.

measurements from S-waves that have both large (>35°) and small (≤ 35°) incidence angles, we adapted the same approach to extract an unambiguous set of splitting parameters that have been determined from earthquakes with a large range of epicentral distances. Long rays may attain horizontal propagation in some parts of the ray path, depending on the ray geometry. Such a horizontal propagation could be sensitive to transversely isotropic media with vertical symmetry axis (e.g., horizontal foliations and sedimentary bedding). These types of media most likely occur in the eastern offshore, where there is an oceanic-plateau with shallow bathymetry, thick continental crust and less tectonic activity [*Davy and Uruski*, 2002]. As found by *Paulssen* [2004], S-waves that travel horizontally through media with slow, vertical axes of hexagonal symmetry, such as flat layered schists and sedimentary sequences, will have their fast polarization direction orthogonal to the ray path.

2.2. Results and Interpretations

In Figure 1a, fast azimuths (ϕ) measured at stations in the western and eastern offshore regions are represented as rose diagrams. We allowed the program to calculate at least three splitting measurements for each event to examine the sensitivity of splitting parameters to different filter bandwidths. Individual rose diagrams are weighted by the number of measurements with that particular azimuth and therefore, the longer the rose segment the higher the number of measurements in that direction. The rose diagrams are normalized according to the number of measurements at each station, but information on the number of events is found in Tables 1 and B1. Because of the configuration of the OBS network and earthquake distribution, splitting measurements on western and eastern OBS mainly sample the anisotropy in the Australian and Pacific lithosphere respectively (Figure 1a).

We extracted a single pair of splitting parameters for each event by using the best filter criterion. The best filter criterion compares the splitting measurements from the three best filters (as measured by the product of the signal-to-noise-ratio) for each event and chooses a single set of splitting parameters if the splitting measurements are similar for all three different filters (Appendix A) [*Savage et al*., 2010]. Figures 1b, 2a, and 2b and Table 1 show these best filter splitting measurements and their station averages. In general,

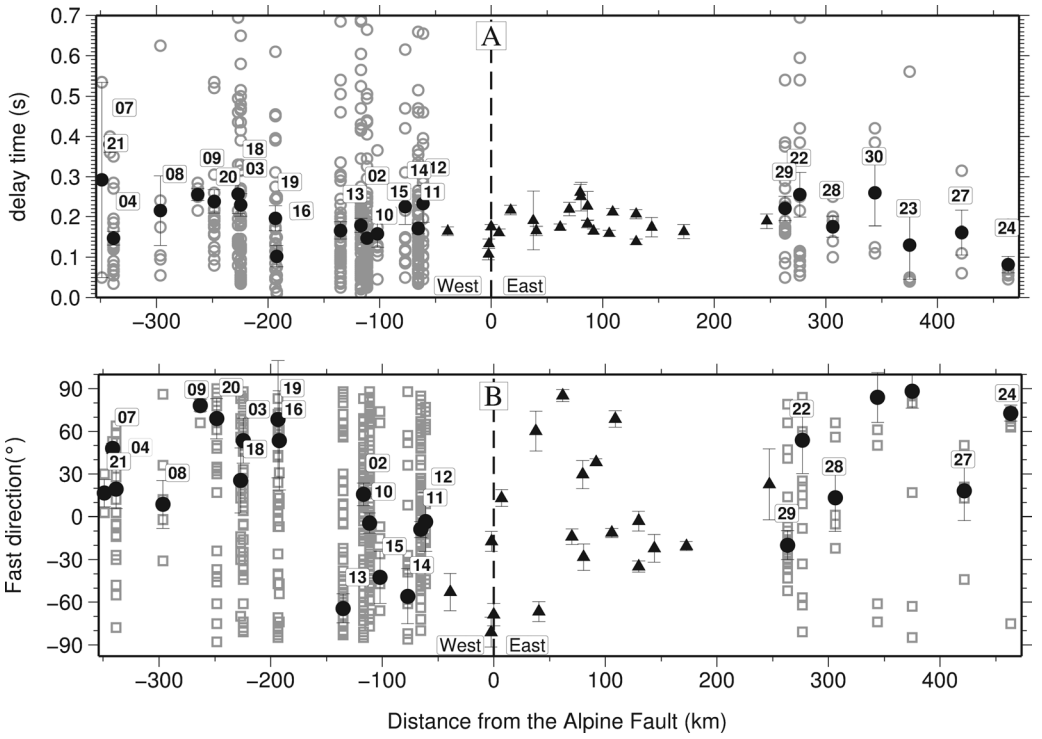

Figure 2. (a) δt (gray open circles) and (b) ϕ (gray open boxes) variations with distance from the Alpine fault. The boxed-numbers represent the OBS station locations across the fault. Mean splitting parameters at each OBS station are marked by the black circles. Black triangles denote the average δt and ϕ estimated at the inland stations [*Karalliyadda and Savage*, 2013], which are located in the central and northern South Island. Error bars indicate the standard errors of the mean splitting parameters at each station, which are much smaller than the scatter because of the reduction of error in the means by a factor of the square root of the number of measurements.

individual splitting delay times (δt) from both sides range from ~0.02 – 0.5 s (Figure 2a) with an average value of 0.25 s. Station ϕ are not spatially consistent throughout the whole region, but patches of spatial consistencies can be seen in the western offshore with a rapid change in ϕ from plate-boundary parallel in the far west to plate-boundary perpendicular at about 150 km from the plate-boundary (Figures 1a, 1b, and 2b).

2.2.1. Splitting Estimation in Western Offshore

The western OBS are distributed up to ~350 km distance from the Alpine fault. Stations are located in three distinct zones (Figure 1): (1) deep ocean basin (Tasman sea) on oceanic crust close to the Puysegur subduction (NZ02, NZ03, and NZ04), (2) central region (southernmost part of the Challenger plateau) in the continental-continental collisional zone near the Alpine fault (where NZ11, NZ10, NZ12, NZ13, NZ14, and NZ15 are located), and (3) northeast and central parts of the Challenger Plateau near paleo-rift systems [*Wood*, 1991]. In the northeast Challenger Plateau (NZ18, NZ20, NZ21,and NZ07), ϕ estimates show prominent plate-boundary parallel (30–70^o) alignment compared to ϕ estimates in the central offshore region that are perpendicular to the plate-boundary. OBS in the deep sea and near by regions (NZ02, NZ03, NZ04, and NZ10) yield a bimodal distribution of ϕ with one mode parallel to the NE-SW alignment. This azimuth is also consistent with the ϕ at stations in the northeast Challenger Plateau (NZ18, NZ07, NZ20). The other mode is roughly NW-SE or NNW-SSE and consistent with the predominant azimuth of the two-modes observed at the central stations (NZ10, NZ11, NZ13, NZ14, NZ15). The *absolute plate motion* (APM) in the Tasman sea region is roughly NW-SE to NNW-SSE, indicating the possibility of asthenospheric flow-governed anisotropy in the region.

From these azimuths alone, it is not clear if the NW-SE ϕ mode in the central stations (NZ15, NZ14, NZ13, NZ12) is a product of asthenospheric flow or has a stress controlled source (e.g., fluid-filled cracks and/or grain-boundary aligned consolidation). The maximum horizontal compressive stress (SH_{max}) direction of the adjacent onshore region is ~115° (Figure 1a) [*Boese et al.*, 2012], which is consistent with the NW-SE trend. If the brittle deformation (e.g., cracks and fractures) associated with the Alpine fault extends into offshore

regions, relatively high compressive stress in this region may have an effect on crustal anisotropy. A rather diffuse, but fault parallel mode (NE-SW) observed at NZ12, NZ13, NZ15 and NZ14 in central offshore suggests that S-wave splitting for some paths in this region is also sensitive to anisotropy due to plate-boundary parallel shear. However, high-frequency local/regional S-phases tend to be more biased toward shallow stress-controlled anisotropy [*Huang et al*., 2011; *Audoine et al*., 2000]. Furthermore, SKS measurements yield plate-boundary parallel ϕ at the same stations, suggesting that deeper plate-boundary shear is occurring [*Zietlow et al*., 2014]. NE-SW ϕ at stations in the northeast Challenger Plateau agrees well with ϕ patterns in the onshore regions of the northern South Island (see section 2.3) [*Karalliyadda and Savage*, 2013]. This implies that the deformation around the transform-translational fault zone in the northern South Island is distributed in a broader region. Another possible explanation for NE-SW ϕ in this region is that fast anisotropic directions align parallel to the NE-SW oriented paleo-rifting (parallel to rift axis) [*Vauchez and Nicolas*, 1991] associated with the Tasman rift system, which are assumed to be preserved throughout the Challenger Plateau [*Wood*, 1991]. The average δt varies between 0.1 and 0.4 s in western offshore regions (Figure 2a). When considering the δt variations across the Alpine fault, there is a slight increase in average station δt (from about 0.17$\pm$0.02 s in the east to 0.26$\pm$0.04 in the west; Table 1) after the 150 km boundary-limit from the Alpine fault (Figure 2a). This could be due to accumulation of the δt along the ray path [*Silver and Chan*, 1991; *Rumpker and Silver*, 1998] and/or sampling of a more pronounced zone of anisotropy at depth by steeply curved ray paths. ϕ estimates display a NE-SW azimuth that is parallel to the plate-boundary (Figure 2b) beyond 150 km limit from the shore.

2.2.2. Splitting Parameter Estimation in Eastern Offshore

OBS on the eastern side are mainly located on the Chatham Rise and the northernmost part of the Campbell Plateau; these regions are considered as continental extensions of the eastern South Island [*Sutherland*, 1999]. Stations in the eastern offshore are far away from most of the earthquakes and, thus, only a few S-phases yield acceptable quality splitting parameters (Figure 1). Null splitting measurements of SKS phases near Chatham Island in the Chatham Rise suggest that the region is almost isotropic [*Klosko et al*., 1999; *Zietlow et al*., 2014].

The station δt averages range from 0.1 to 0.3 s (Figure 2a) and these values most likely represent a shallow crustal origin. NZ29 and NZ28 show NW-SE ϕ that are consistent with the ϕ from adjacent onshore stations (section 2.3). S-waves could also be sensitive to anisotropy due to horizontal layering if the ray paths attain a longer horizontal propagation due to ray-curvature from source to station [*Paulssen*, 2004]. ϕ perpendicular to ray paths as observed on some event-station pairs in the eastern offshore (Figure 3) may indicate such an effect ($\sim$40 % of the total ϕ are within 70° – 90° of the *back azimuth* (BAZ), Figure 3). Chatham Rise stations (NZ23 and NZ24) have smaller average delays ($\sim$0.1 s or less) compared to those measured at other stations (Figure 1b). Most of the measurements made at these stations have ϕ nearly perpendicular to the ray paths. This suggests that those ray paths may sample the local/shallow anisotropy that represents a crustal source such as shallow sedimentary layers. Therefore, complex fast azimuth patterns in eastern offshore (Figure 3) may reflect varying path directions through the horizontally layered media. Low δt ($\sim$0.2 s) can be attributed to either cancellation of anisotropy due to changes in the orientation of the symmetry axis, and flipping between fast and slow waves along the ray path or to crustal resplitting owing to shallow upper-crustal anisotropy.

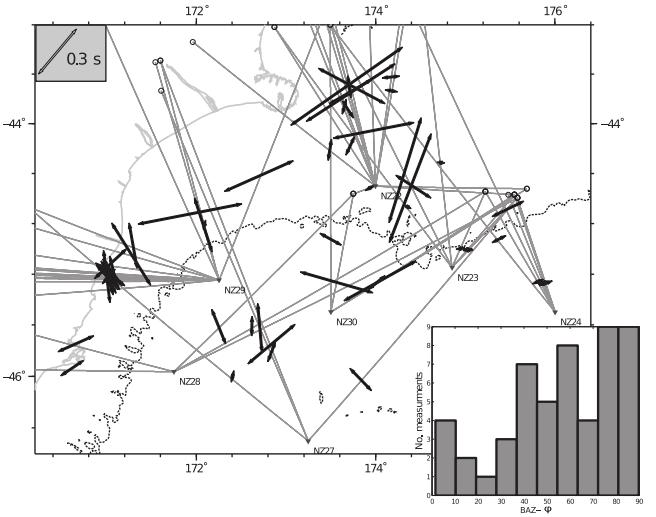

Figure 3. Zoomed-in view of the individual measurements (good quality) in eastern offshore South Island. Measurements are plotted at one-quarter of the epicentral distance from the station to avoid overlapping. Histogram shows the number of measurements versus an acute-angle between BAZ and ϕ (FD). Note that about 40% of the fast azimuths (ϕ) are perpendicular or high-angle (70°–90°) to the horizontal projection of the ray paths (gray lines).

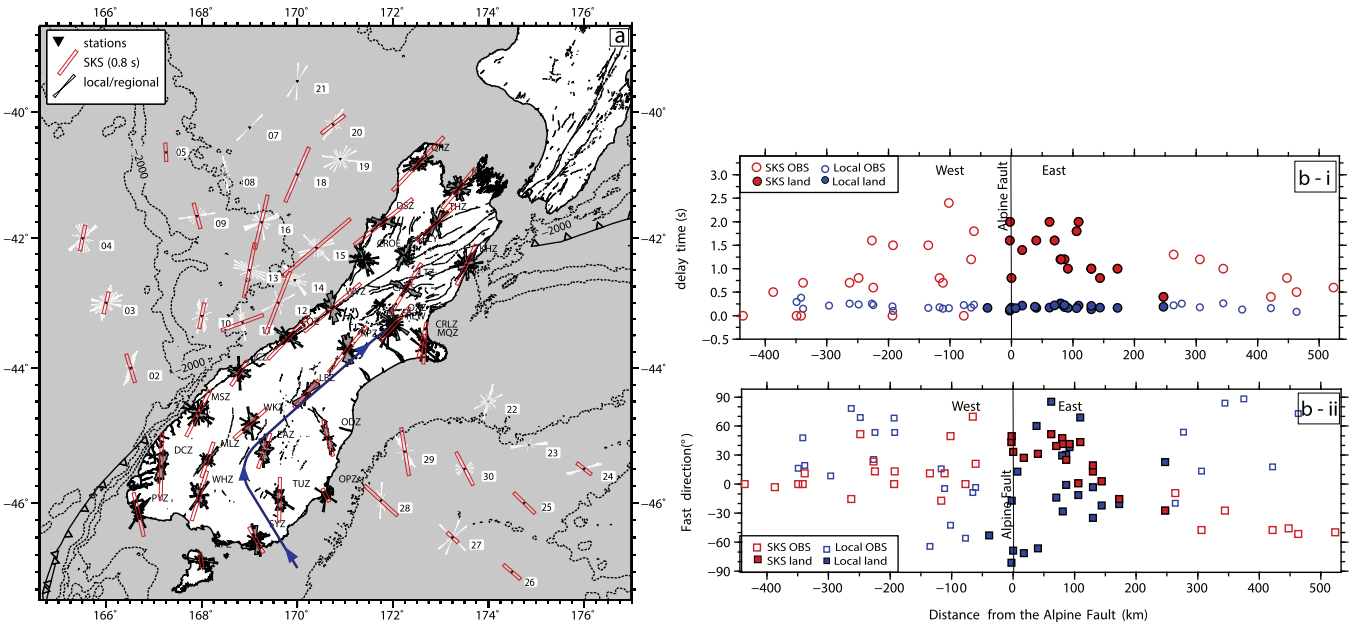

Figure 4. (a) A map-view comparison between local/regional ϕ (rose diagrams) and SKS splitting measurements (red open-bars) [*Zietlow et al.*, 2014] on-land and offshore. Gray and white rose diagrams denote the on-land and offshore measurements respectively. The size of the SKS bars are proportional to δt. The blue line with arrows indicates changes in general trend of the ϕ toward the plate boundary. (b) The comparison of SKS and local splitting parameters ((**b-ii**)$-\phi$ and (**b-i**)$-\delta$t) across the Alpine fault. Land and offshore measurements are marked by the filled and open symbols respectively. δt (circles) and ϕ (squares) are plotted at the station location relative to the Alpine fault (marked in black solid line).

2.3. Characterizing the Anisotropic Structure

To fully characterized the observed anisotropy in the region, we compare splitting measurements with previous results of SKS splitting, determine spatial averages of ϕ and apply the 3-D splitting tomography technique.

2.3.1. Comparison With SKS Splitting Measurements

We compare fast azimuths from regional and local splitting with the recent SKS splitting study by *Zietlow et al.* [2014] using the same OBS network, which also reanalyzed the on-land SKS splitting measurements using a recent data set. SKS measurements show a clear deflection in the alignment of ϕ from fault-parallel (NE-SW) near the fault to N-S or NW-SE (at high angle to the fault) alignment in the central-east and southeast of the South Island (red bars in Figure 4a and red squares in Figure 4bii). This change may reflect the change in orientation of the deep anisotropy. A similar trend can be observed from the local/regional splitting (the blue line with arrow heads in Figure 4a) mainly in the southeastern side of the plate-boundary. The plate-boundary and relative plate motion (RPM) parallel/subparallel ϕ within ~80–90 km distance east of the plate-boundary (gray rose diagrams at MLZ, WKZ, LBZ, RPZ stations in Figure 4a) likely indicates anisotropy due to plate-boundary parallel shear. This plate-boundary parallel ϕ is approximately consistent with SKS ϕ, although this is not clear from the local ϕ at stations on the Alpine fault due to multi-mode ϕ.

The prominent trend of ϕ from the local/regional S-wave splitting observed at stations NZ29, NZ28, NZ30 (white rose diagrams in Figure 4a) and eastern on-land South Island stations (EAZ, ODZ, TUZ, SYZ, OPZ) is roughly consistent with the general SKS ϕ trend (NNW-SSE) in the region, implying that the long ray paths of the S-waves may have propagated through the deep region of the upper-lithosphere and/or asthenosphere and captured the anisotropy due to flow in the asthenosphere or fossilized anisotropy in the deep upper-lithosphere (compare ray paths in Figure 5c). The prominent local ϕ alignment at NZ18, NZ20, NZ10, NZ03, and NZ04 on the western side is roughly consistent with SKS ϕ, but in the central-west offshore (NZ11, NZ12, and NZ13), the main local/regional ϕ are oblique to the SKS fast trends at those stations.

2.3.2. Spatial Patterns of ϕ

Both onshore [*Karalliyadda and Savage*, 2013; *Karalliyadda*, 2014] and offshore (this study) splitting measurements (Figure 4) are integrated to provide constraints on the spatial patterns of ϕ in the entire plate-boundary zone of the South Island. The spatial analysis used a total of 4838 ray paths (2130 events) recorded on 56 stations throughout the study region. Figures 5a and 5c show the map view and depth

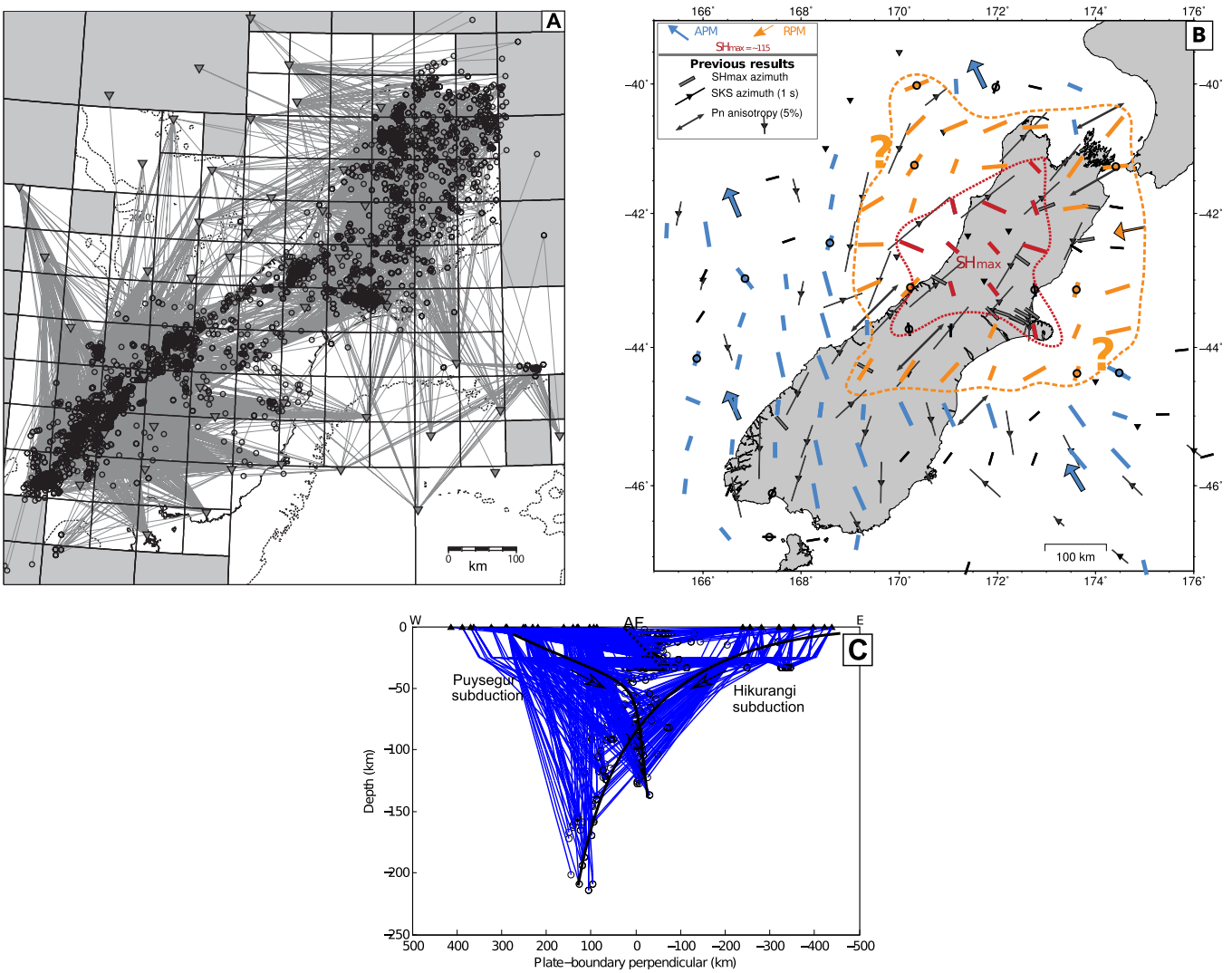

Figure 5. (a) Ray paths, events, and station distribution and quadtree grids that were used to determine spatial averages. Note the inactive grids are marked in gray color. (b) Spatial averages of ϕ ($\bar{\phi}_b$) of offshore and onshore splitting measurements from quadtree gridding with minimum grid size of 50 km. Bars are color coded according to the consistent patterns that are likely aligned with the RPM/Alpine Fault (yellow), APM (blue) and SH_{max} (red) directions. $\bar{\phi}_b$ that are not consistent with those regional trends and/or anti-correlated (angular difference $>45°$) with the expected regional trends are denoted by black bars. Long and short colored bars indicate the well (angular difference $\leq 15°$) and moderately ($15° <$angular difference $\leq 45°$) correlated $\bar{\phi}_b$. The bars with black circles denote $\bar{\phi}_b$ with standard error (SE) $>25°$. Note gray color symbols (see the left-top legend) represent SH_{max} [*Townend et al.*, 2012], SKS ϕ [*Zietlow et al.*, 2014] and P_n anisotropy [*Savage et al.*, 2007a] measurements from previous studies. (c) Cross section (E-W) of the ray-traced ray paths (blue lines) through AK135 velocity model across the plate-boundary. Black open-circles and triangles show the earthquake locations and station distribution. The approximate locations of the Alpine Fault (AF) and two subduction systems (Hikurangi and Puysegur) are marked in dotted and bold black lines, respectively.

cross section of the ray-traced ray paths of the S-phases used in the spatial analysis. Two-dimensional spatial averages are determined from spatially defined grids (Figure 5a) from quadtree gridding (TESSA) [*Johnson et al.*, 2011]. The criteria for quadtree gridding are that if the number of rays in each grid is greater than 40 then those grids are further divided in to smaller grid sizes (Figure 5a). The minimum grid-spacing is set-up to be 50 km. Grids with less than 5 rays are discarded from the analysis to obtain reliable average measurements. Then, the fast direction from each splitting measurement is assigned to each grid block through which the ray travels between the event and station. In each grid block, the average fast direction ($\bar{\phi}_b$) and standard error of $\bar{\phi}_b$ are determined from all the ϕ measurements within each grid block using circular statistics [*Philipp*, 2009; *Mardia*, 1972].

$\bar{\phi}_b$ in Figure 5b are color coded according to the regional consistencies considering the uncertainties. $\bar{\phi}_b$ are considered to align with RPM (relative plate motion – yellow)/Alpine Fault, APM (absolute plate motion – blue) and SH_{max} (red) directions. $\bar{\phi}_b$ that are not consistent with those regional trends and/or are anti-

correlated (angular difference >45°) with the expected trends in those regions are highlighted in black. Long and short colored bars indicate the well (angular difference ≤ 15°) and moderately (15° < angular difference ≤ 45°) correlated $\bar{\phi}_b$. The bars with black circles denote $\bar{\phi}_b$ with standard error (SE) > 25°. According to these spatially defined average ϕ, the spatial distribution of anisotropic structure appears to be characterized by three distinct anisotropic sources. In the region with yellow bars, ϕ are parallel/subparallel to the relative plate motion (RPM = ~70°) [*DeMets et al*., 1994] direction (thin arrows in Figure 5b) and strike of the Alpine Fault (~55°); the region with blue bars: ϕ (outermost- ~330° ± 45° are consistent with the absolute plate motion (APM) [*Gripp and Gordon*, 2002] direction (bold blue arrows in Figure 5b). The zone with red bars: ϕ (~115° ± 45°) are consistent with SH_{max} azimuth (bold-gray bars) [*Townend et al*., 2012].

Except in the SH_{max} governed zone, local/regional ϕ are mostly aligned with the SKS fast azimuths (gray bars with triangles in Figure 5b) in other regions, implying either a deep source of anisotropy or crust-mantle coupled anisotropy. Yellow bars are distributed in a wide region across the upper-central and northern South Island (Figure 5b), indicating plate-boundary shear. However, in the central South Island, the plate-boundary parallel zone tends to be masked by a zone with a plate-boundary oblique azimuth (zone with red bars) that is aligned with the SH_{max} direction in that region [*Townend et al*., 2012] or the axis of shortening [*Houlié and Stern*, 2012]. The denser shallow ray paths in this region appear to sample the shallow anisotropic structure more heavily than sparse deep S-wave paths, which sample the deeper structure. Alternatively, deeper ray paths could also be more sensitive to the shallow structure because of the high-frequency content of those S-phases (Figure 5c). The outer-most zone with blue bars has a very diffuse pattern, but agrees with SKS azimuths of the near by regions (Figure 5b). This zone is likely controlled by the present-day asthenospheric flow or by preserved fabrics in the deep upper-lithosphere (the minimum depth limit of the lithosphere-asthenosphere boundary in South Island is ~100 km; *Stern et al*. [2000]). The boundary limit of yellow and blue zones (yellow dashed lines in Figure 5b) consistently follows the changes in SKS ϕ throughout the plate-boundary zone.

2.3.3. 3-D Splitting Tomography

We apply shear wave splitting tomography [*Abt and Fischer*, 2008] to resolve the complex splitting in the region. This method assumes that the observed splitting is governed solely by the preferred alignment of the intrinsically anisotropic minerals. The method has three main steps: 1) model parametrization, 2) forward modeling of splitting and, 3) inversion of shear-wave splitting parameters. The detailed description of these steps are given in *Abt and Fischer* [2008]. Here we briefly discuss how we adapt the above three steps to obtain the final inversion model solution.

The model space of this data set is defined so that it includes all stations and events that were used to obtain shear-wave splitting parameters (Figure 6a). We chose grid blocks with 25 km^3 volume to characterize the 3-D space (i.e., along the plate-boundary (400 km), across plate-boundary (475 km) and maximum depths of 250 km). Larger grid spacings resulted in a lack of small-scale structure and smaller grid spacings led to too few ray paths in each block and also to prohibitively lengthy inversion runs. A total of 7020 ray paths (2982 events and 56 stations) were used for the inversion (Figure 6a). The scale of our study region is relatively larger than the regions that have been investigated using this technique previously [*Abt et al*., 2009].

This analysis uses an average starting model (Figure 6b). After ray-tracing through the model space, the average starting model is determined from the 3-D weighted averages of ϕ in each block (ϕ_b) [see *Abt and Fischer*, 2008, Appendix A]. Depth slices through the average starting model (Figure 6b) are given in Figure B5. This 3-D averaging is an extended version of the 2-D ϕ_b determined from TESSA (Figure 5b) considering both spatial and depth distribution of the ray-paths. We assume a hexagonal crystal symmetry that is simulated from the orthorhombic single-crystal elastic constants of olivine and ortho-pyroxene as described in *Abt and Fischer* [2008]. Thus, in each block, crystallographic orientations are defined by two angles that represent the horizontal azimuth of the a-axis [1 0 0] (θ) and the plunge of the a-axis (ψ). We use this mantle material approximation throughout the model, with the recognition that the crust is actually controlled by micaceous mineral or stressed-aligned cracks, and different types of olivine will align with different orientations. Therefore the results will be an approximation, but the orientation of the inferred fast direction of anisotropy should be robust. Therefore when we discuss the interpretations of the a-axes returned in the inversion, we use the term fast direction instead of a-axis alignment. The average fast direction in each block is used as a proxy for the a-axis orientation of crystals in the horizontal plane. b-axis in the initial model is

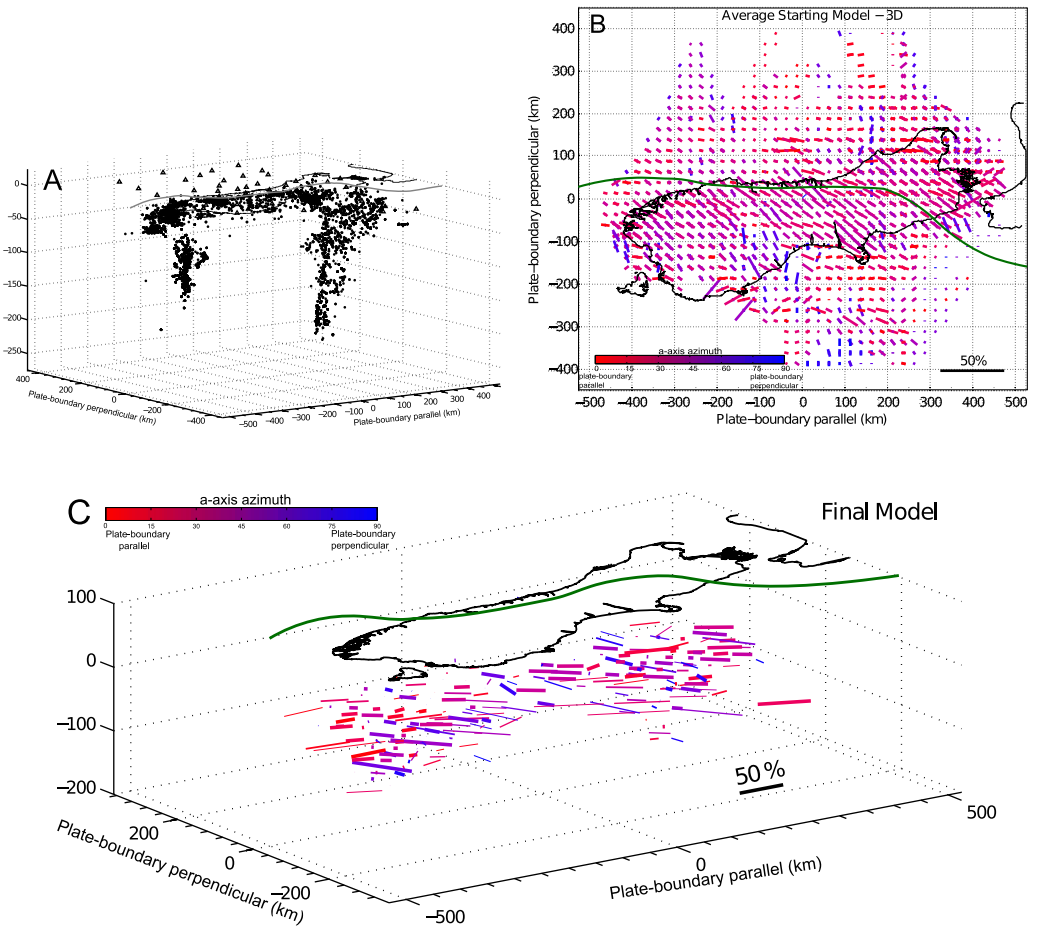

Figure 6. (a) Stations and event distribution with in the model space. An approximate position of the plate boundary is marked by the gray line. (b) 2-D view of the three-dimensionally averaged starting model. (c) 3-D view of the resolved final model (green line denotes the approximate position of the plate boundary). The colored bars represent the a-axis azimuth and the length of bars indicates strength of anisotropy in each block (%) as determined by the equation (1). a-axis alignments are color coded relative to the plate-boundary parallel (red) and perpendicular (blue). Thickness of the bars are scaled by the resolution matrix diagonal element values ($^{dia}R_m$), so that thicker vectors are better resolved than the thinner bars (e.g., thinnest bars: $0.25 \leq {}^{dia}R_m < 0.5$ and thickest bars: $0.9 \leq {}^{dia}R_m < 1$).

considered to be vertical. The strength of anisotropy of each ray (α_r) is a relative measure of $\delta t^{observed}$ and $\delta t^{predicted}$. $\delta t^{predicted}$ is calculated from the S-wave splitting per kilometer when the ray propagates vertically through a system with horizontally aligned a-axis azimuths and with the olivine elastic constants and finally, multiplying splitting per kilometer by the actual path length of the ray (L_r). Then, the weighted (weighted by the path-length in each block; $L_{r,b}$) averages of strength of anisotropy in each block (α_b) is determined from equation (1) [see *Abt and Fischer*, 2008, Appendix A]. $\overline{\alpha_b}$ varies between 0 and 100 %.

$$\overline{\alpha_b} = \frac{\sum_{r=1}^{n} \left(\frac{\delta t^{obs.}}{\delta t^{pred.}} \right) \cdot (L_{r,b})}{\sum_{r=1}^{n} L_{r,b}} \times 100 \tag{1}$$

The method uses damped least-squares inversion iteratively to minimize the misfit between observed and predicted splitting parameters [e.g., *Tarantola*, 2005]. Forward calculation of splitting parameters (predicted splitting) is done with the particle motion perturbation method [*Abt and Fischer*, 2008] for each ray path in the model. The effect of 3-dimensionally varying anisotropic structure on the rays when they travel from earthquakes to stations is determined by taking into account crystallographic orientations and the strength of anisotropy of each block that the ray propagates through. The Christoffel equation is used to determine the polarization directions and the phase velocities (and hence delay times) in each block using the model parameters.

The average ϕ misfit gradually decreases during the inversion process and reaches a global minimum around the 50^{th} iteration (Figure B2ai). The average δt misfit reaches a global minimum value within the first 10 iterations, and then increases, with a further increase after the damping relaxation at the 40^{th} iteration (Figure B2aii). This suggests that the delay times are not well defined, and we concentrate our interpretation more on the fast directions. Figures B3a and B3b compare the ϕ of circular histograms that are produced from the observed splitting measurements (Figure B3a) and the predicted splitting measurements (Figure B3b) using the final model (Figure 6c). The predicted measurements produce less scattered circular histograms compared to the observed measurements. At some stations, the predicted trends agree well with the observed trends (e.g., OBS stations 07, 20, 19, 18, 10, 11 in the west and 27, 23 and 30 in the southeast and land stations DSZ, LTZ, JCZ, TUZ) or their averages (Figure B4b). At other stations the predicted trends either agree with only one mode of ϕ distribution (e.g., OBS stations 08, 16, 04, 22, and land stations CROE, MSZ, WHZ, MLZ, WKZ), or disagree with the observed measurements (e.g., OBS stations 21, 05, 02, 29, land stations DCZ, THZ, CRLZ, MQZ). The predicted splitting may represent the deeper anisotropy intrinsic to the upper-most mantle lithosphere.

Figure 6c displays the well resolved parts of the 3-D model with the fast direction alignment. Figures 7a–7d show 2-D depth slices through the 3-D model space (compare with the depth slices through the average starting model displayed in Figure B5). At crustal and upper-most mantle depths (the maximum measured crustal depth in the South Island is ~48 km; *Bourguignon et al*. [2007]) the fast direction aligns close to the plate-boundary (especially in the two subduction zones), indicating alignment of crustal minerals (e.g., mica) and plate-boundary parallel shear (Figures 7a and 7b). However, the resolution of the offshore regions and at deeper depths is poor. In the central plate-boundary zone the majority of alignments are at high angle to the plate-boundary and these measurements are consistent the with 2-D averaged ϕ_b (Figure 5b). In the northern South Island, the majority of fast azimuths are aligned with the plate-boundary and the Hikurangi trench at depths (Figures 7c and 7d), suggesting trench-parallel governed anisotropy. In southern South Island, the trench-oblique alignment dominates at deeper parts (e.g., Figure 7d). The dip of the axes of symmetry was not well resolved and so we do not consider it in our interpretations.

3. Discussion

Local/regional events recorded on the OBS network offshore South Island allowed us to resolve the complex anisotropic structure associated with AUS-PAC plate-boundary zone with enhanced resolution. Both long and short S-wave paths used in this analysis are likely sensitive to different structures at depth. Frequency dependence of splitting measurements within this data set was minimal. However, compared to simpler results from longer period (>10 s period) SKS measurements [*Zietlow et al*., 2014], complex splitting could be partly due to sensitivity of the high frequency S-phases (average ~5 Hz) from local earthquakes to the shallow anisotropic structure. Figure 8 shows the possible ray paths that could sample different sources of anisotropy in the central South Island plate-boundary zone. If we assume a broad asymmetric lithospheric shear-zone parallel to the plate-boundary as suggested by *Duclos et al*. [2005] (possibly extending down to the asthenosphere) (Figure 8), the majority of S-waves of deep events with long ray paths are likely to sample the anisotropy of this shear-zone (Figure 5c and red ray paths in Figure 8). Thus, they will yield plate-boundary parallel ϕ unless anisotropy at shallow depth is strong. Near-vertical shear-planes in the vicinity of the plate-boundary, can be tilted to produce dipping anisotropy or can be rotated to the horizontal away from the plate-boundary. In such cases the strength of splitting may vary. This may also be the case if ray segments are tilted (i.e., not near vertical) in vertically aligned media. In the regions where this shear is not distributed or strong, S-phases of the deep subduction events (≥100 km) will be sensitive to present-day asthenospheric flow, resulting in APM parallel/subparallel fast directions. In the southern South Island, especially in offshore and eastern on-land, this could be the case (Figure 5c). S-phases from shallow and shorter ray paths mostly reside in the shallow crust and they will be sensitive to crustal anisotropy (Figure 5b and blue ray paths in Figure 5c). In the central South Island, the majority of events occur at shallow crustal depths (Figure 8). Thus, those S-phases can be sensitive to both shallow shear-induced anisotropy and crustal stress or/structure induced anisotropy, depending on the geometry of ray propagation.

We have identified a zone with SH_{max} parallel ϕ in the northern-central/central South Island, where we do not have a good depth resolution. This stress-controlled zone diminishes in the southern-central and the southern

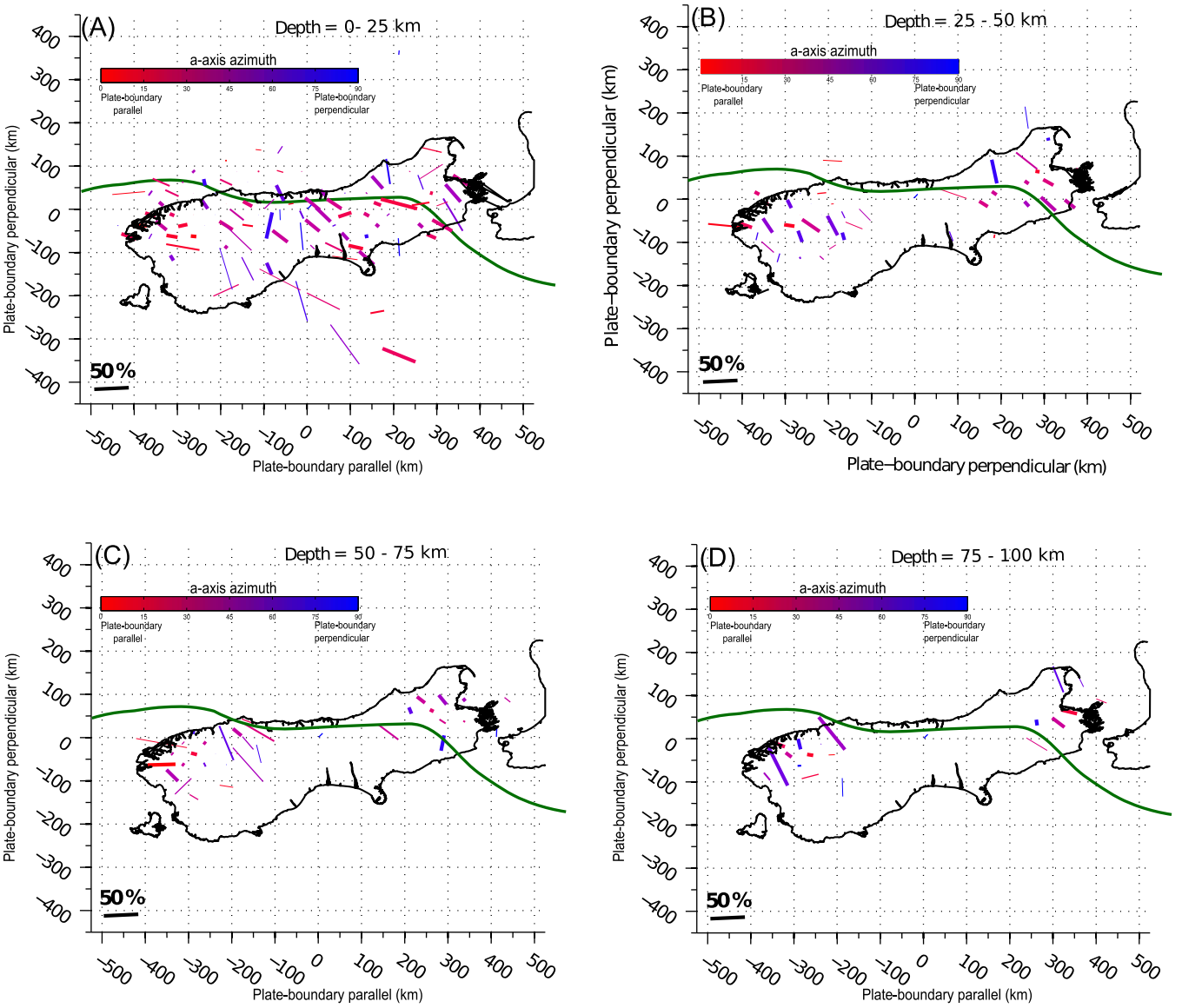

Figure 7. Depth slices (depth range = (a) 0–25 km, (b) 25–50 km, (c) 50–75 km, (d) 75–100 km.) through the 3-D final model. The approximate location of the plate-boundary is marked by the green line. Red to blue colored bars indicate the a-axis orientation (fast direction) of the hexagonal crystals relative to the plate-boundary orientation. Refer Figure 6c for more information.

South Island, and plate-boundary parallel ϕ or APM subparallel ϕ become dominant (Figure 5b). This diminution of stress control could be due to the presence of deep ray paths that sample deep anisotropy.

The 2-D spatial analysis of ϕ suggests that there is a plate-boundary induced shear zone beneath the shallow stress-induced anisotropic zone in the central South Island (Figure 5b). Comparing with SKS splitting measurements [*Zietlow et al*., 2014], we suggest this zone is distributed in the west-offshore at lithospheric depths and does not extend into east-offshore at lithospheric depths (Figure 8). However, it is also possible that this zone is broadly distributed in the deep-lithosphere (deeper than 90 km), where we do not have ray-coverage, and extends into the asthenosphere. Nevertheless, SKS splitting suggests that such a shear-induced body is absent in the eastern offshore regions at deeper depths and is mainly governed by the present-day asthenospheric flow [*Zietlow et al*., 2014] (Figure 4). As constrained by *Zietlow et al*. [2014], the width of plate-boundary induced shear is about 100 – 200 km. Local/regional splitting from this study suggests a broad shear zone exists in the northern South Island beneath the plate-boundary and transitional fault zone.

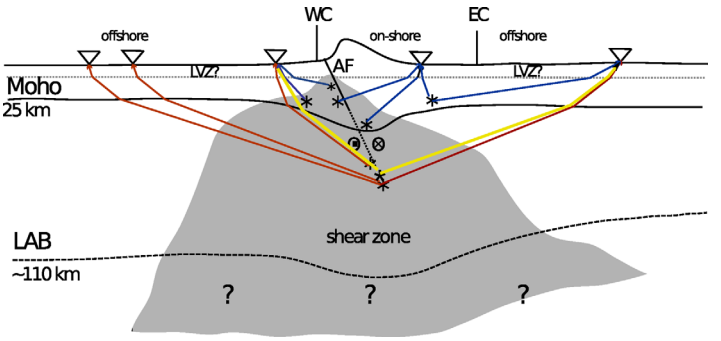

Figure 8. Schematic explaining the ray configuration and sensitivity of ray paths to different anisotropic zones (WC - West Coast, EC - East Coast, AF - Alpine Fault, LVZ - Low Velocity Zone). Red-colored ray paths likely sample the plate-boundary parallel shear-zone (gray region), whereas blue ray paths may be sensitive to more shallow sources (e.g., crustal anisotropy). The yellow rays indicate the deep S-phases that could be sensitive to the uppermost anisotropy.

Splitting parameters can be complex, yet systematically vary (i.e., periodic variations) with BAZ if dipping or layered anisotropy exists [*Rumpker and Silver*, 1998; *Babuska et al*., 1993; *Silver and Savage*, 1994]. These systematic variations in splitting parameters with BAZ have been observed with long-period S-waves (e.g., SKS) with very good backazimuthal coverage, and two-layer and dipping models have been investigated with such waves at station SNZO in southern North Island [*Marson-Pidgeon and Savage*, 2004]. But local S-waves splitting analysis in the inland South Island by *Karalliyadda and Savage* [2013] found no significant correlation between splitting parameters and BAZ. Observed complex splitting measurements by *Karalliyadda and Savage* [2013] were attributed to the combined effects of depth variations of anisotropy, dipping anisotropy, and crustal heterogeneities. The 3-D inversion analysis takes into account both multiple layers and dipping axes of symmetry [*Abt and Fischer*, 2008]. However, because of the lack of backazimuthal coverage (Figure 1b) at most of the offshore stations and possible depth variation of anisotropy in the region, the existence of dipping layers or multilayer anisotropy may not be accurately investigated using the individual station measurements in our data set. The spatial analysis of ϕ clearly suggests that there are both spatial and depth contribution of anisotropy. S-wave paths likely encounter more than a single layer of anisotropy, or plunging anisotropic layers, when they reach the station. Even if the anisotropy is characterized by a horizontal symmetry axis, the S-phases may not sample the full effect of the properties of the anisotropic medium because of the ray geometry (e.g., curved ray paths). At least some parts of the long and shallow ray paths are likely sensitive to transverse isotropy with vertical symmetry axes. In that case, observed variable ϕ can be attributed to the effects of both transverse isotropy with vertical symmetry and horizontal symmetry (i.e., azimuthal anisotropy). Depending on how rays propagate in the layered media and the anisotropic symmetry, splitting may reflect an integrated effect at the receiver. Measured low δt, therefore, probably represents either the anisotropy of the upper most layer (crustal source; e.g., yellow ray paths in Figure 8) or the integrated effect of the variable anisotropy along the ray path.

Figures 6, 7, and B2–B5 present the first attempt at a 3-D inversion for anisotropy in the South Island. The model uses only the local earthquakes and does not incorporate frequency-dependent effects. The method should include effects due to propagation through dipping symmetry axes and multiple blocks/layers. The predicted splitting from the model returns less scatter than is observed in the real measurements (Figure B3). This is probably because the shallow crustal splitting varies more rapidly than the 25 km^3 blocks used in the inversion and is averaged within the blocks. Because of the simplified assumption of mantle material throughout the model space and the homogeneous distribution of mantle material within each volume block (25 km^3), the predicted measurements from the model do not encounter the small-scale variations of anisotropy and shallow crustal anisotropy. Thus, the predicted measurements show consistent ϕ trends, which are most likely biased toward the deeper anisotropy. We note particularly that the calculated splitting through the model for the OBS stations (Figure B3b) matches well to the SKS measurements at the OBS stations on the continental crust (East and West of New Zealand; Figure 4a), but not on the oceanic crust on stations 02, 03 and 04. We recommend further examination of 3-D models with more powerful computer systems to examine more fully the effects of different starting models and material approximations.

4. Conclusions

Local and regional splitting analysis in the offshore South Island together with land-based splitting measurements allows us to constrain the anisotropy distribution in the plate-boundary zone of South

Table B1. The Number of Measurements From Different Grading Criteria

Criteria[a]	No. Measurements
AB grade/all[b]	2076
AB grade/$\lambda_{max} > 5/\delta t \leq 0.7$ s	1300
AB grade/best-filter/$\delta t \leq 0.7$ s	1390
AB grade/best-filter/$\lambda_{max} > 5/\delta t \leq 0.7$ s	547

[a]See appendix A for grading criteria.
[b]Measurements from all filters with SNR >3.

Island. Depending on the ray distribution, S-phases appear to be sensitive to three distinct anisotropic layers at depths in the region. The spatial analysis of splitting measurements suggests that there is a broad zone of shear adjacent to the plate-boundary fault, at least in the central-north and northern South Island. Because of the limited deep earthquakes in the central South Island and possible frequency dependent and/or multilayer effects, the depth extent of this shear zone is not well constrained. Nevertheless, plate boundary parallel ϕ at some stations far away (~200 km) from the plate-boundary suggest that steeply curved ray paths from deep events (50 – 90 km) are likely sensitive to a shear zone in the upper lithosphere (above ~90 km). This implies that deformation around the plate-boundary zone in South Island is distributed widely in the lithosphere, in agreement with the deformation distribution predicted by the thin viscous sheet model (i.e., continuous lithospheric deformation as result of deformation on the vertical shear planes with little or no depth variation in strain rates) [*Molnar et al.*, 1999]. Except in the central South Island stress-governed anisotropic zone, these spatial constraints are also consistent with the SKS splitting patterns. 3-D splitting tomography suggests that the anisotropy in the two subduction settings is governed by plate-boundary shear at crustal depths and trench parallel flow in the mantle-lithosphere.

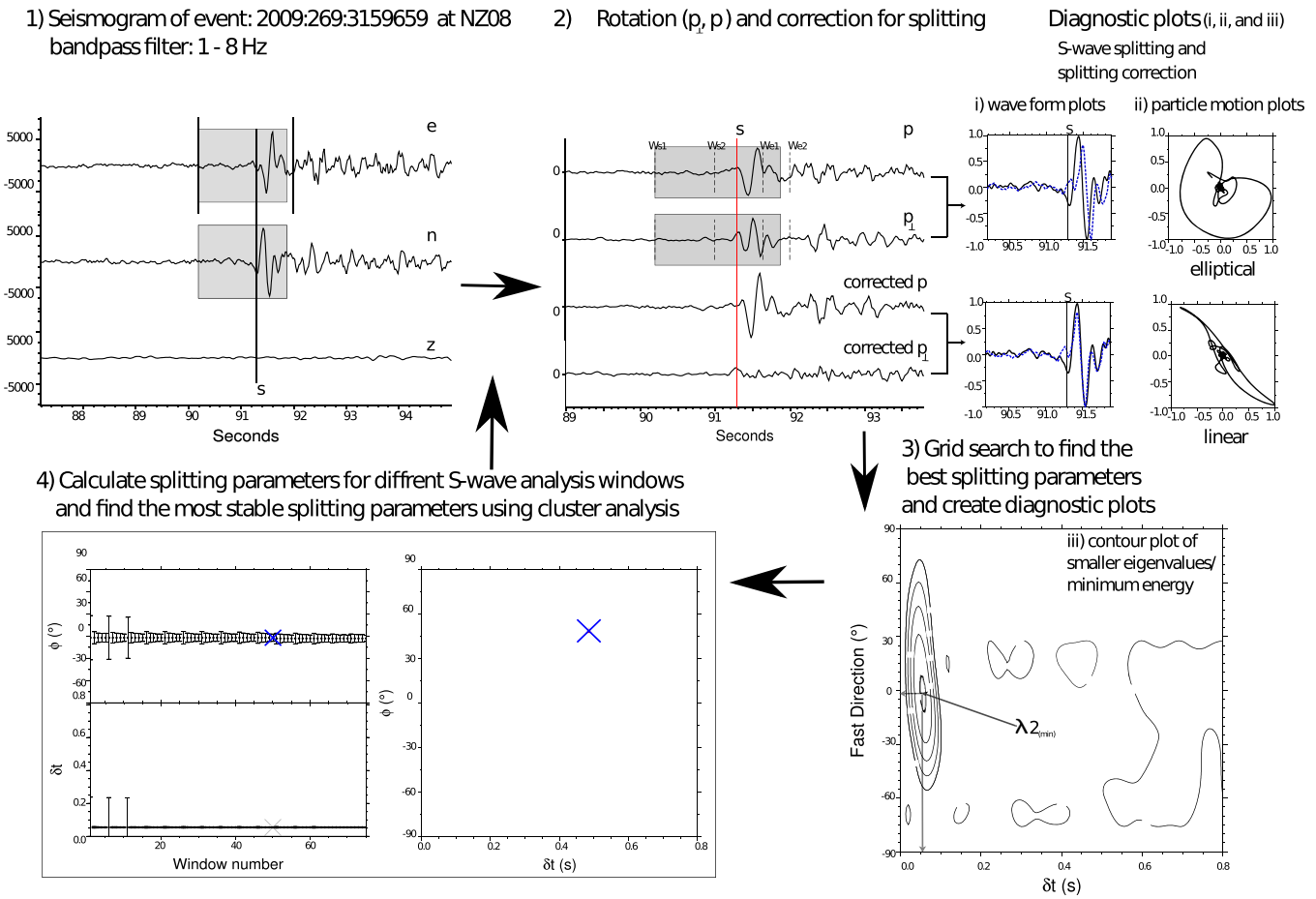

Figure B1. The main steps of measuring S-wave splitting parameters using MFAST [*Savage et al.*, 2010]: (1) Picking the S-arrival and filtering the three-component seismogram (e,n, and z) (2) Measuring splitting parameters by rotating (p and $p_\perp$), shifting (corrected p and $p_\perp$) seismograms and calculating eigenvalues of the covariance matrix, which is calculated from the corrected components. Here dashed lines indicate the minimum starting time and maximum end time of the different S-wave analysis windows (3) Repeat step 2 applying a grid search over ϕ and δt to find the smallest second eigenvalue ($\lambda_{2(min)}$). $\lambda_{2(min)}$ is denoted by the blue cross, which is placed within the 95% confidence limit (dark black line) in the contour plots (diagnostic plot iii) of second eigenvalues (or minimum energy). The diagnostic plots of wave form and particle motion plots show the correction for splitting using the best splitting parameters at $\lambda_{2(min)}$. (4) Repeat step 2 and step 3 for different shear-wave analysis windows that are defined between minimum (W_{s1})/maximum (W_{s2}) starting time and minimum (W_{e1})/maximum(W_{e2}) end time (step 2) and find the most stable splitting parameters from the cluster analysis [*Teanby et al.*, 2004b].

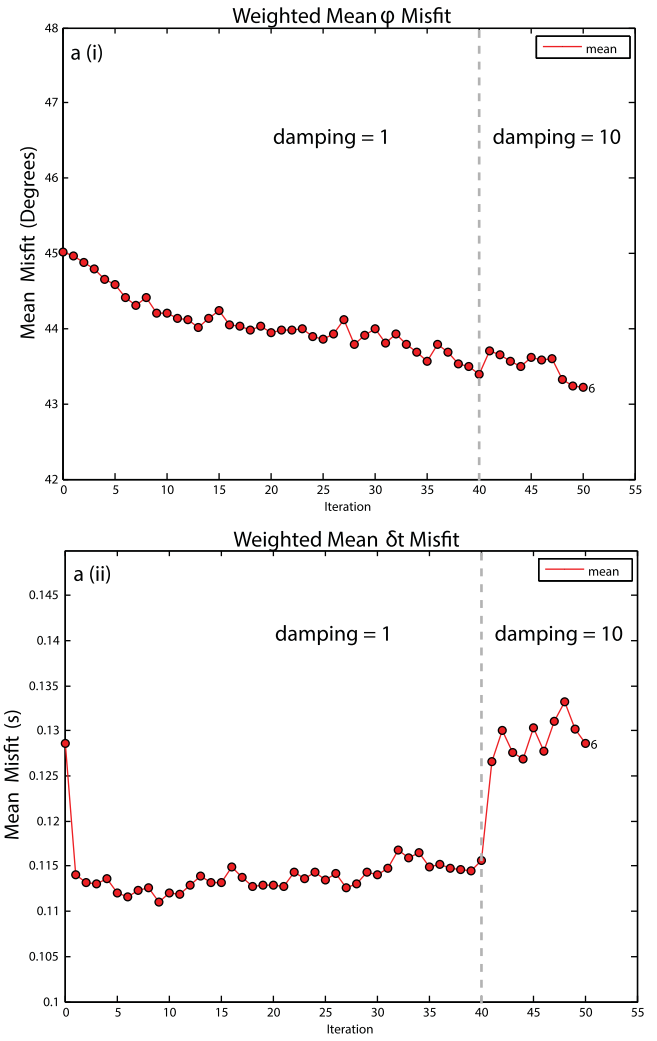

Figure B2. The changes in weighted mean misfit of (i) ϕ and (ii) δt during the inversion with 50 iterations. Note that the model instability (i.e., sudden increase in δt misfit) due to change in damping from 1 to 10 at the 40th iteration.

Appendix A: Grading and Selection of Spitting Measurements

A1. AB Grade

A and/or B graded (i.e., good and best quality) splitting measurements as defined by *Savage et al.* [2010]. AB grading agrees with the following criteria:

SNR >3, δt $<0.8*tlag_{max}$ ($tlag_{max}$ is the maximum δt for grid search), maximum error in $\phi < 25^{circ}$, if it is not a null measurement, and if the measurement graded as A or B in the cluster grading [*Teanby et al.*, 2004b]. Note that the A grade criteria (a. SNR >4, b.δt $<0.8*tlag_{max}$, c. not null and $d\phi$ (error) $<10^{\circ}$) are a subset of AB grade criteria.

A2. Highest Grade

The highest quality splitting measurements are AB grade measurements with high numbers of error contours. The error contours are determined from the eigenvalues of corrected covariance matrices for each trial value of ϕ and δt. The minimum eigenvalue is chosen as the best measurement for that window, and the eigenvalues are normalized so that a value of 1 is the 95% confidence interval and higher values are multiples of that. The best measurements have large numbers of contour intervals, indicating that the 95% confidence is well separated from the larger, poorer, values. λ_{max} is the maximum value on the contour plot of eigenvalues of the corrected covariance matrix [*Savage et al.*, 2010]. The highest quality has $\lambda_{max}>5$, indicating dense error contours. We used the best filter, AB grade splitting measurements (explained above) with $\lambda_{max}>5$ (the highest quality) to analyze the spatial distribution of splitting measurements.

A3. Best Filter Measurement

We use the sel_bestmeas code in the Mfast package [*Savage et al.*, 2010] to determine the best single measurement from among the measurements of the three best filters. If there is more than one acceptable splitting measurement for a given S-wave, the routine compares the splitting measurements for each filter and eliminates those with measurements that are too different from each other. Splitting measurements are considered to be too different if the time difference is greater than the $tlag_{max}/8$ ($tlag_{max}$ is defined in the AB grading) or if the angular distance is greater than $\pi/8$. If the measurements are similar, the measurement with the smallest error bars is chosen.

Appendix B: Additional Figures and Tables

The Appendix B consists of additional figures and tables related to shear-wave splitting method (Mfast – Figure B1), 3-D splitting tomography (Figure B2, Figure B3, Figure B4, and Figure B5), and splitting measurements (Table B1).

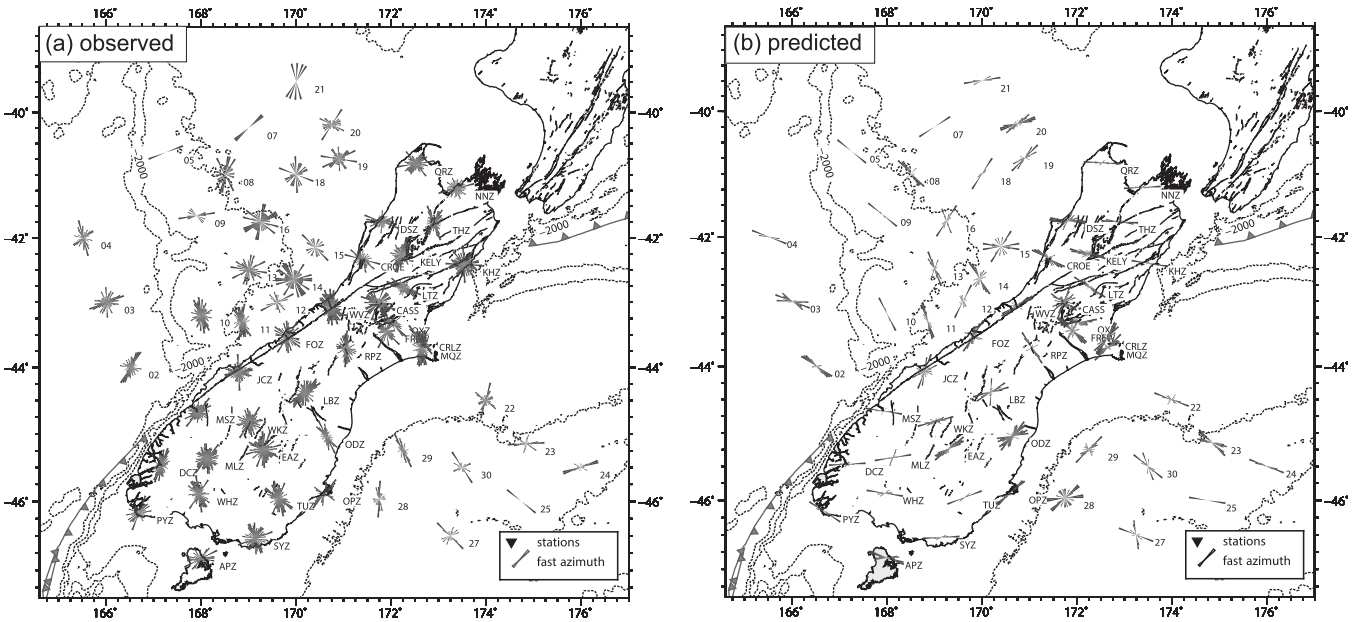

Figure B3. Comparison of the observed and predicted splitting measurements. The comparison of the predicted and observed average splitting parameters estimated from these measurements are given in figure B4. (a) The circular histograms of fast azimuths plotted at the station locations from the observed splitting measurements. (b) The circular histograms of fast azimuths from the predicted splitting measurements.

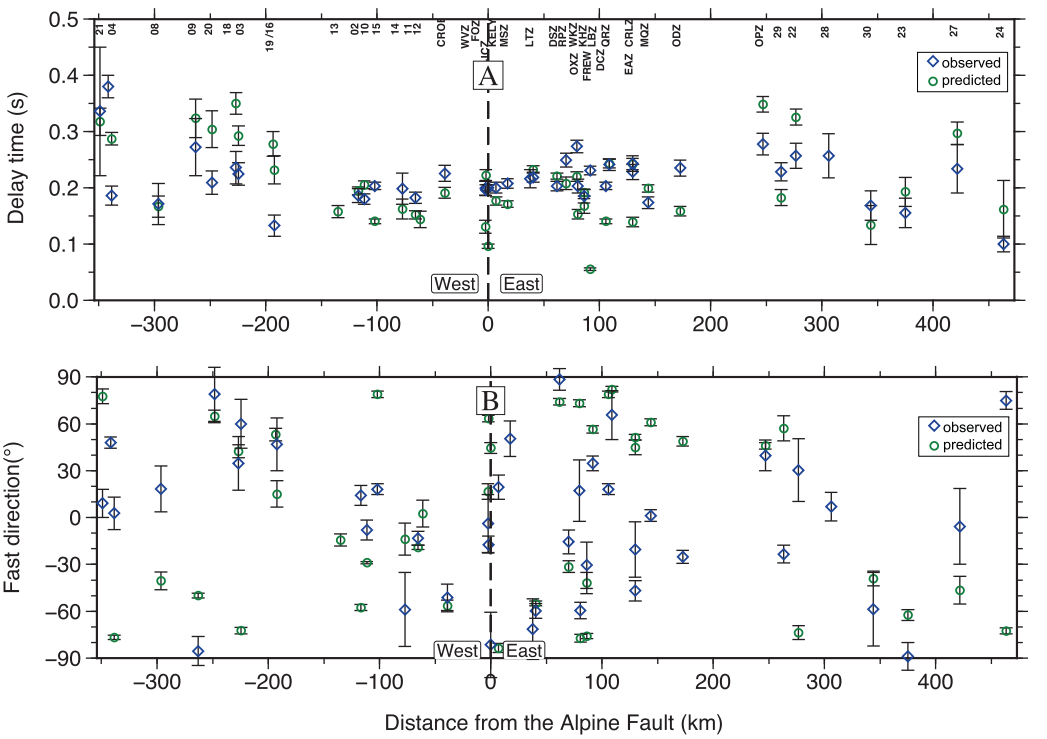

Figure B4. Comparison of the average splitting measurements that are determined from the observed and predicted splitting measurements displayed in Figure B3. The observed (diamonds – blue) and the predicted (circles – green) station averages are plotted at the station location with respect to the Alpine fault. Error bars indicate the standard error (SE) of the average splitting parameters at each station. Note that fast azimuths with SE $\leq 25°$ are shown.

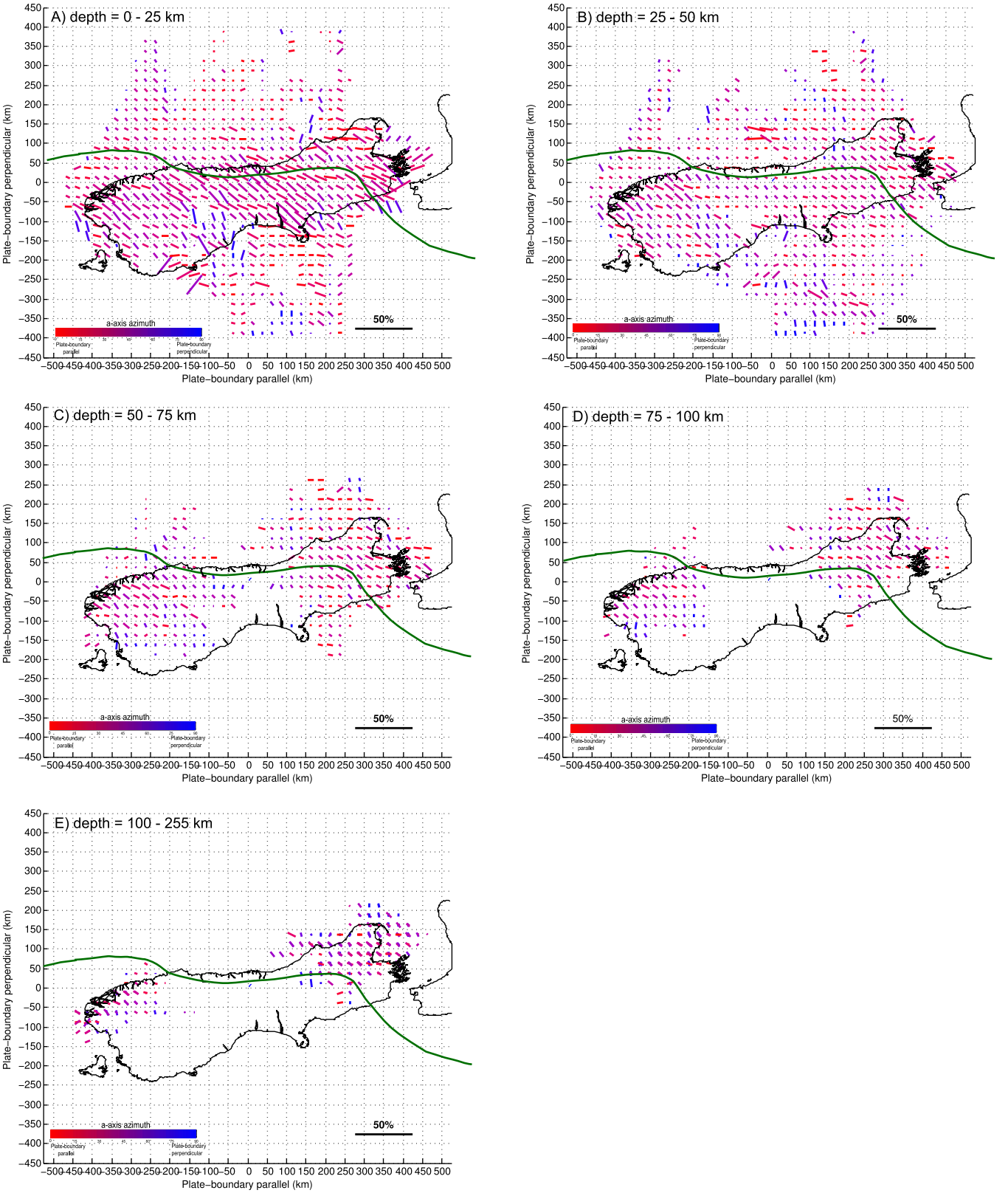

Figure B5. Depth slices (depth range = (a) 0–25 km, (b) 25–50 km, (c) 50–75 km, (d) 75–100 km, (e) 100–225 km) through the starting model (Figure 6-B). Red to blue colored bars indicate the a-axis orientation of the hexagonal crystals relative to the plate-boundary orientation. Refer to Figure 6c for more details.

Acknowledgments
We would like to thank the MOANA-OBS project, captain and R/V Thomas G. Thompson cruise (TN229-2009), R/V Roger Revelle cruise (RR1002-2010) and science groups. The OBS sensors used for this analysis were supplied by the United States National Ocean Bottom Seismograph Instrumentation Pool. We thank VUW PhD scholarship and grants from the NZ Foundation for Research, Science and Technology and the Marsden Fund for giving financial support. Special thanks to K. M. Fischer for supplying the splitting tomography program. We also thank B. Fry, E. Smith and M. Long for their constructive reviews on the PhD-thesis chapter that was later converted into this manuscript. We are grateful to G. Rumpker and an anonymous reviewer for their valuable comments. The instruments and waveform data used in this study are archived at the IRIS Data Management Center. The earthquake information were obtained from the GeoNet project (http:\\www.geonet.org.nz). The splitting data and tomography input files are available from the authors upon request (sapi.karal@outlook.com and martha.savage@vuw.ac.nz).

References

Abt, D. L., and K. M. Fischer (2008), Resolving three-dimensional anisotropic structure with shear wave splitting tomography, *Geophys. J. Int.*, *173*, 859–886.

Abt, D. L., K. M. Fischer, G. A. Abers, W. Strauch, J. M. Protti, and V. Gonzlez (2009), Shear wave anisotropy beneath Nicaragua and Costa Rica: Implications for flow in the mantle wedge, *Geochem. Geophys. Geosyst.*, *10*, Q05S15, doi:10.1029/2009GC002375.

Audoine, E., M. K. Savage, and K. Gledhill (2000), Seismic anisotropy from local earthquakes in the transition region from a subduction to a strike-slip plate boundary, New Zealand, *J. Geophys. Res.*, *105*(B4), 8013–8033.

Babuska, V., J. Plomerova, and J. Sileny (1993), Models of seismic anisotropy in the deep continental lithosphere, *Phys. Earth Planet. Inter.*, *78*(3-4), 167–191.

Baldock, G., and T. Stern (2005), Width of mantle deformation across a continental transform: Evidence from upper mantle (pn) seismic anisotropy measurements, *Geology*, *33*(9), 741–744.

Beavan, J., et al. (1999), Crustal deformation during 1994–1998 due to oblique continental collision in the central Southern Alps, New Zealand, and implications for seismic potential of the alpine fault, *J. Geophys. Res.*, *104*(B11), 25,233–25,255.

Boese, C. M., J. Townend, E. G. C. Smith, and T. A. Stern (2012), Microseismicity and stress in the vicinity of the Alpine Fault, central Southern Alps, New Zealand, *J. Geophys. Res.*, *117*, BO2302, doi:10.1029/2011JB008460.

Boness, N. L., and M. D. Zoback (2004), Stress-induced seismic velocity anisotropy and physical properties in the SAFOD pilot hole in Parkfield, CA, *Geophys. Res. Lett.*, *31*, L15S17, doi:10.1029/2003GL019020.

Booth, D., and S. Crampin (1985), Shear-wave polarizations on a curved wavefront at an isotropic free-surface, *Geophys. J. R. Astron. Soc.*, *83*(1), 31–45.

Bourguignon, S., T. A. Stern, and M. K. Savage (2007), Crust and mantle thickening beneath the southern portion of the southern Alps, New Zealand, *Geophys. J. Int.*, *168*(2), 681–690.

Cox, S., and R. Sutherland (2007), Regional geological framework of South Island, New Zealand, and its significance for understanding the active plate boundary, in *A Continental Plate Boundary: Tectonics at South Island, New Zealand*, vol. 175, edited by D. Okaya, T. Stern, and F. Davey, pp. 19–46, AGU, Washington, D. C.

Davy, T., and C. Uruski (2002), Results of the 2001 deep seismic survey of the Chatham rise and Hikurangi plateau and implication for petroleum exploration, New Zealand Petroleum Exploration Conference Proceedings, Ministry of Commerce, Wellington, Feb.

DeMets, C., R. G. Gordon, D. F. Argus, and S. Stein (1994), Effect of recent revisions to the geomagnetic reversal time scale on estimates of current plate motions, *Geophys. Res. Lett.*, *21*(20), 2191–2194.

Duclos, M., M. K. Savage, A. Tommasi, and K. R. Gledhill (2005), Mantle tectonics beneath New Zealand inferred from SKS splitting and petrophysics, *Geophys. J. Int.*, *163*(2), 760–774.

Ellis, S., J. Beavan, and D. Eberhart-Phillips (2006), Bounds on the width of mantle lithosphere flow derived from surface geodetic measurements: Application to the central southern Alps, New Zealand, *Geophys. J. Int.*, *166*(1), 403–417.

Flesch, L. M., W. E. Holt, P. G. Silver, M. Stephenson, C. Y. Wang, and W. W. Chan (2005), Constraining the extent of crust-mantle coupling in central asia using gps, geologic, and shear wave splitting data, *Earth Planet. Sci. Lett.*, *238*(1-2), 248–268.

Gripp, A. E., and R. G. Gordon (2002), Young tracks of hotspots and current plate velocities, *Geophys. J. Int.*, *150*(2), 321–361.

Houlié, N., and T. Stern (2012), A comparison of GPS solutions for strain and sks fast directions: Implications for modes of shear in the mantle of a plate boundary zone, *Earth Planet. Sci. Lett.*, *345*, 117–125.

Huang, Z., D. Zhao, and L. Wang (2011), Frequency-dependent shear-wave splitting and multilayer anisotropy in northeast Japan, *Geophys. Res. Lett.*, *38*, L08302, doi:10.1029/2011GL046804.

Johnson, J. H., M. K. Savage, and J. Townend (2011), Distinguishing between stress-induced and structural anisotropy at Mount Ruapehu volcano, New Zealand, *J. Geophys. Res.*, *116*, B12303, doi:10.1029/2011JB008308.

Karalliyadda, S. (2014), S-wave splitting in the transpressional zone of New Zealand plate-boundary: Implications for deformation and dynamics, PhD thesis, School of Geography, Environment and Earth Sciences, Victoria Univ. of Wellington, Wellington, New Zealand.

Karalliyadda, S. C., and M. K. Savage (2013), Seismic anisotropy and lithospheric deformation of the plate-boundary zone in South Island, New Zealand: Inferences from local s-wave splitting, *Geophys. J. Int.*, *193*(2), 507–530, doi:10.1093/gji/ggt022.

Karato, S., et al. (1989), Seismic anisotropy: Mechanisms and tectonic implications, in *Rheology of Solids and of the Earth*, edited by S. Karato, and M. Toriumi, pp. 393–422, Oxford University Press, Oxford, U. K.

Klosko, E. R., F. T. Wu, H. J. Anderson, D. Eberhart-Phillips, T. V. McEvilly, E. Audoine, M. K. Savage, and K. R. Gledhill (1999), Upper mantle anisotropy in the New Zealand region, *Geophys. Res. Lett.*, *26*(10), 1497–1500.

Little, T. A., M. K. Savage, and B. Tikoff (2002), Relationship between crustal finite strain and seismic anisotropy in the mantle, pacific-Australia plate boundary zone, South Island, New Zealand, *Geophys. J. Int.*, *151*(1), 106–116.

Mardia, K. V. (1972), *Statistics of Directional Data*, Academic, London, U. K.

Marson-Pidgeon, K., and M. K. Savage (2004), Modelling shear wave splitting observations from Wellington, New Zealand, *Geophys. J. Int.*, *157*(2), 853–864, doi:10.1111/j.1365-246X.2004.02274.x.

Molnar, P., et al. (1999), Continuous deformation versus faulting through the continental lithosphere of New Zealand, *Science*, *286*(5439), 516–519.

Moore, M., P. England, and B. Parsons (2002), Relation between surface velocity field and shear wave splitting in the South Island of New Zealand, *J. Geophys. Res.*, *107*(B9), 2198, doi:10.1029/2000JB000093.

Nicolas, A. (1993), Why fat polarization direction of sks seismic waves are parallel to mountain belts, *Phys. Earth Planet. Inter.*, *78*, 337–342.

Nicolas, A., and N. I. Christensen (1987), Formation of anisotropy in upper mantle peridotite: A review, in *Composition, Structure and Dynamics of the Lithosphere-Asthenosphere System*, vol. 16, edited by K. Fuchs and C. Froidevaux, pp. 111–123, AGU, Washington, D. C.

Nuttli, O. (1961), The effect of the earth's surface on the s wave particle motion, *Bull. Seismol. Soc. Am.*, *51*(2), 237–246.

Otsuki, K. (1978), On the relationship between the width of shear zone and the displacement along fault, *J. Geol. Soc. Jpn.*, *84*, 661–669.

Paulssen, H. (2004), Crustal anisotropy in southern California from local earthquake data, *Geophys. Res. Lett.*, *31*, L01601, doi:10.1029/2003GL018654.

Philipp, B. (2009), Circstat: A MATLAB toolbox for circular statistics, *J. Stat. Software*, *31*(10), 1–21.

Rumpker, G., and P. G. Silver (1998), Apparent shear-wave splitting parameters in the presence of vertically varying anisotropy, *Geophys. J. Int.*, *135*, 790–800.

Savage, K., M. Duclos, and K. Marson-Pidgon (2007a), Seisimic anisotropy in South Island, New Zealand, in *A Continental Plate Boundary: Tectonics at South Island, New Zealand*, vol. 175, edited D. Okaya, T. Stern and F. Davey, AGU, Washington, D. C.

Savage, M. K. (1999), Seismic anisotropy and mantle deformation: What have we learned from shear wave splitting?, *Rev. Geophys.*, *37*(1), 65–106.
Savage, M. K., T. Ohminato, Y. Aoki, H. Tsuji, and S. M. Greve (2010), Stress magnitude and its temporal variation at mt. asama volcano, japan, from seismic anisotropy and GPS, *Earth Planet. Sci. Lett.*, *290*(3-4), 403–414.
Scherwath, M., T. Stern, A. Melhuish, and P. Molnar (2002), Pn anisotropy and distributed upper mantle deformation associated with a continental transform fault, *Geophys. Res. Lett.*, *29*(8), 1175, doi:10.1029/2001GL014179.
Silver, P. G., and W. W. Chan (1991), Shear-wave splitting and subcontinental mantle deformation, *J. Geophys. Res.*, *96*(B10), 16,429–16,454.
Silver, P. G., and M. K. Savage (1994), The interpretation of shear-wave splitting parameters in the presence of two anisotropic layers, *Geophys. J. Int.*, *119*(3), 949–963, doi:10.1111/j.1365-246X.1994.tb04027.x.
Skemer, P., J. M. Warren, and G. Hirth (2012), The influence of deformation history on the interpretation of seismic anisotropy, *Geochem. Geophys. Geosyst.*, *13*, Q03006, doi:10.1029/2011GC003988.
Stachnik, J., A. Sheehan, D. Zietlow, Z. Yang, J. Collins, and A. Ferris (2012), Determination of New Zealand ocean bottom seismometer orientation via Rayleigh-wave polarization, *Seismol. Res. Lett.*, *83*, 704–712, doi:10.1785/0220110128.
Stern, T., P. Molnar, D. Okaya, and D. Eberhart-Phillips (2000), Teleseismic p wave delays and modes of shortening the mantle lithosphere beneath south island, New Zealand, *J. Geophys. Res.*, *105*(B9), 21,615–21,631.
Sutherland, R. (1999), Basement geology and tectonic development of the grater New Zealand region: Interpretation from regional magnetic data, *Tectonophysics*, *308*, 341–362.
Tarantola, A. (2005), *Inverse Problem Theory and Methods for Model Parameter Estimation*, Society for Industrial and Applied Mathematics, Philadelphia, doi:10.1137/1.9780898717921.
Teanby, N. A., J. M. Kendall, and M. Van der Baan (2004b), Automation of shear-wave splitting measurements using cluster analysis, *Bull. Seismol. Soc. Am.*, *94*(2), 453–463.
Townend, J., S. Sherburn, R. Arnold, C. Boese, and L. Woods (2012), Three-dimensional variations in present-day tectonic stress along the Australia-pacific plate boundary in New Zealand, *Earth Planet. Sci. Lett.*, *353–354*, 47–59, 10.1016/j.epsl.2012.08.003.
Tsuji, T., J. Dvorkin, G. Mavko, N. Nakata, T. Matsuoka, A. Nakanishi, S. Kodaira, and O. Nishizawa (2011), Vp/vs ratio and shear-wave splitting in the nankai trough seismogenic zone: Insights into effective stress, pore pressure, and sediment consolidation, *Geophysics*, *76*(3), WA71–WA82.
Vauchez, A., and A. Nicolas (1991), Mountain building strike-parallel motion and mantle anisotropy, *Tectonophysics*, *185*, 183–201.
Volti, T., Y. Kaneda, S. Zatsepin, and S. Crampin (2005), An anomalous spatial pattern of shear-wave splitting observed in ocean bottom seismic data above a subducting seamount in the nankai trough, *Geophys. J. Int.*, *163*(1), 252–264.
Wessel, A. (2010), Automatic shear wave splitting measurements at Mt. Ruapehu volcano, New Zealand, MSc thesis, School of Geography, Environment and Earth Sciences, Victoria Univ. of Wellington, Wellington, New Zealand.
Wood, R. (1991), Structure and seismic stratigraphy of the western challenger plateau, *N. Z. J. Geol. Geophys.*, *34*, 1–9.
Yang, Z., A. Sheehan, J. A. Collins, and G. Laske (2012), The character of the seafloor ambient noise recorded offshore New Zealand: Results from the Moana ocean bottom seismic experiment, *Geochem. Geophys. Geosyst.*, *13*, Q10011, doi:10.1029/2012GC004201.
Zietlow, D. W., A. F. Sheehan, P. H. Molnar, M. K. Savage, G. Hirth, J. A. Collins, and B. H. Hager (2014), Upper mantle seismic anisotropy at a strike-slip boundary: South Island, New Zealand, *J. Geophys. Res. Solid Earth*, *119*, 1020–1040, doi:10.1002/2013JB010676.